First-principles study of the giant magnetic anisotropy energy in bulk Na_4IrO_4

Di Wang,[1] Feng Tang,[1] Yongping Du,[2,1] and Xiangang Wan[1,*]

[1]*National Laboratory of Solid State Microstructures, Collaborative Innovation Center of Advanced Microstructures, College of Physics, Nanjing University, Nanjing 210093, China*

[2]*Department of Applied Physics, Nanjing University of Science and Technology, Nanjing 210094, China*

(Received 19 July 2017; revised manuscript received 9 October 2017; published 30 November 2017)

In 5*d* transition-metal oxides, novel properties arise from the interplay of electron correlations and spin-orbit interactions. Na_4IrO_4, where the 5*d* transition-metal Ir atom occupies the center of the square-planar coordination environment, has attracted research interest. Based on density functional theory, we present a comprehensive investigation of electronic and magnetic properties of Na_4IrO_4. We propose the magnetic ground-state configuration, and find that the magnetic easy axis is perpendicular to the IrO_4 plane. The magnetic anisotropy energy (MAE) of Na_4IrO_4 is found to be giant. We estimate the magnetic parameters in the generalized symmetry-allowed spin model, and find that the next-nearest-neighbor exchange interaction J_2 is much larger than other intersite exchange interactions and results in the magnetic ground-state configuration. The numerical results reveal that the anisotropy of interatomic spin-exchange interaction is quite small and the huge MAE comes from the single-ion anisotropy. This compound has a large spin gap but very narrow spin-wave dispersion, due to the large single-ion anisotropy and quite small intersite exchange couplings. We clarify that these remarkable magnetic features are originated from its highly isolated and low-symmetry IrO_4 moiety. We also explore the possibility to further enhance the MAE.

DOI: 10.1103/PhysRevB.96.205159

I. INTRODUCTION

It is well known that the Coulomb interaction is of substantial importance in 3*d* electron systems, while the spin-orbit coupling (SOC) in these compounds is quite small [1,2]. However, the SOC and electronic correlation in 5*d* electrons have comparable magnitudes. The delicate interplay between electronic interactions, strong SOC, and crystal-field splitting can result in strongly competing ground states in these materials [3–5]. Thus, recently, 5*d* transition-metal (especially Ir or Os) oxides have attracted intensive interest and a great number of exotic phenomena have been observed experimentally or proposed theoretically, e.g., the $J_{\text{eff}} = 1/2$ Mott state [6–8], topological insulators [9–11], the Kitaev model [12], Weyl semimetals [13], high-T_c superconductivity [14–16], axion insulators [17], quantum spin liquids [18,19], Slater insulators [20], ferroelectric metals [21,22], etc. The possible mechanism about the metal-insulator transition in $NaOsO_3$ has also been discussed [23–26].

In all the aforementioned systems, the 5*d* ions lie in the octahedral environment of the O ions. In addition to this common coordination geometry, Na_4IrO_4, where the Ir atom occupies the center of the square-planar coordination environment, has also been synthesized [27]. By using density functional theory (DFT) calculations, Kanungo [28] *et al.* reveal that the relative weak Coulomb repulsion of Ir ions plays a key role in the stabilization of the ideal square-planar geometry of the IrO_4 moiety in Na_4IrO_4. Located at the center of an ideally square-planar IrO_4 oxoanion, the 5*d* electrons of Ir ions in Na_4IrO_4 do not display the $J_{\text{eff}} = 1/2$ configuration [28]. Moreover, the common 5*d* transition-metal oxides own the face-sharing (or edge- or corner-sharing) structure of oxygen octahedrons, while the square-planar IrO_4 oxoanion in Na_4IrO_4 is quite isolated. Therefore, exploring the possible exotic properties of Na_4IrO_4 is an interesting problem.

Recently, there has been considerable research interest in studying materials with a large magnetic anisotropy energy (MAE) since large MAE is desirable for magnetic devices. Most of them are two-dimensional materials or adatoms on surfaces—for example, Co atoms deposited on the Pt (111) surface [29], Fe or Mn atoms absorbed on the CuN surface [30], and Co or Fe atoms on the Pd or Rh (111) surface [31]. In addition, Rau *et al.* [32] found a giant MAE for the Co atoms absorbed on top of the O sites of the MgO (001) surface. Generally, the bulk materials exhibit relatively small MAE of a few μeV [33,34] while anisotropy energies are larger by about three orders of magnitude for multilayers and surface systems [34]. MAE originates from the interaction of the atom's orbital magnetic moment and spin angular moment; thus, an important factor of MAE is the strength of SOC, which increases from 3*d* to 5*d* metals. The symmetry in Na_4IrO_4 is low, while the Ir-Ir distance is quite large due to the isolated nature of IrO_4 moiety. Considering these factors, large MAE is expected in Na_4IrO_4.

In this paper, based on first-principles calculations, we systematically study the electronic and magnetic properties of Na_4IrO_4. Our numerical results show that the Ir-5*d* bands are quite narrow, and the bands around the Fermi level are mainly contributed by d_{xy}, d_{yz}, and d_{zx} orbitals. We propose that the antiferromagnetic-1 (AFM-1) state as shown in Fig. 4 is the ground-state configuration. Due to the isolated IrO_4 moiety, the magnetic moments are quite localized. The magnetic easy axis is perpendicular to the IrO_4 plane, and the MAE of Na_4IrO_4 is found to be giant. The magnetic parameters in a generalized symmetry-allowed spin model have been estimated, and the results show that the next-nearest-neighbor J_2 (shown in Fig. 1) dominates over the others, consequently resulting in the magnetic ground-state configuration. We find the anisotropy of interatomic spin-exchange couplings is relatively small, and the huge MAE comes from the single-ion

*Corresponding author: xgwan@nju.edu.cn

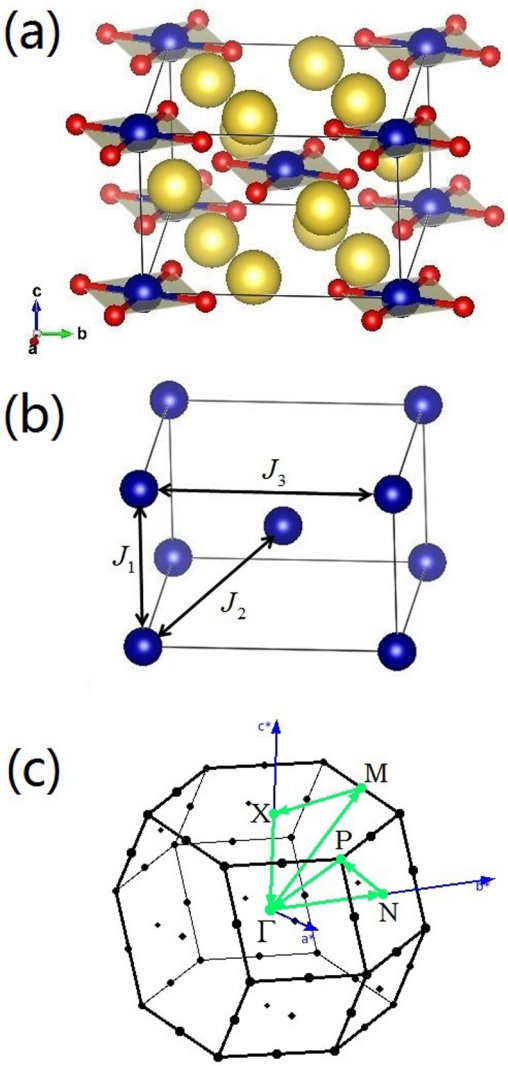

FIG. 1. (a) Crystal structure of Na_4IrO_4. The yellow, blue, and red balls represent the Na, Ir, and O ions, respectively. (b) The nearest-neighbor, next-nearest-neighbor, and third-nearest-neighbor exchange interactions for Ir magnetic moments are shown by J_1, J_2, and J_3, respectively, which are the parameters in the Heisenberg model $H = \sum_{i<j} J_{ij} S_i \cdot S_j$. (c) Brillouin zone of bulk Na_4IrO_4.

anisotropy. This compound has a large spin gap but very narrow spin-wave dispersion. We also clarify the physical mechanism of these novel magnetic properties, and suggest that substituting Ir by an Re atom can further enhance the MAE significantly.

This paper is organized as follows. In Section II we describe the crystal structure for Na_4IrO_4 and the calculational method. The band-structure details and magnetic properties are described in Sec. III. Section IV contains the spin model of our calculations and discussion. In Sec. V, we consider a more general Hamiltonian to analyze the origin of MAE. The suggestion to enhance the MAE is shown in Sec. VI. Finally, the paper is concluded in Sec. VII.

II. METHOD AND CRYSTAL STRUCTURE

The electronic band-structure and density-of-states (DOS) calculations have been carried out by using the full potential linearized augmented plane-wave method as implemented in the WIEN2K package [35]. Local spin-density approximation (LSDA) is widely used for various 4*d* and 5*d* transition-metal oxides (TMO) [6,7,13,17,36], and we therefore adopt it as the exchange-correlation potential. A $9 \times 9 \times 15$ k-point mesh is used for the Brillouin-zone integral. Using the second-order variational procedure, we include the SOC [37], which has been found to play an important role in the 5*d* system. The self-consistent calculations are considered to be converged when the difference in the total energy of the crystal does not exceed 0.01 mRy. Despite the fact that the 5*d* orbitals are spatially extended, recent theoretical and experimental work has given evidence on the importance of Coulomb interactions in 5*d* compounds [3–5]. We utilize the LSDA + U scheme [38] to take into account the effect of Coulomb repulsion in the 5*d* orbital. We vary the parameter U between 2.0 and 4.0 eV and find that the essential properties are independent of the value of U.

As shown in Fig. 1, Na_4IrO_4 crystallizes in the tetragonal structure (space group $I4/m$) [27]. The lattice constants of Na_4IrO_4 are $a = 7.17$ Å and $c = 4.71$ Å [27]. There is only one formula unit in the primitive unit cell, and the nine atoms in the unit cell are located at three nonequivalent crystallographic sites: Ir atoms occupy the 2*a* position, (0,0,0), while both Na and O reside at the 8*h* sites, (x,y,z) [27]. The square-planar IrO_4 oxoanion occurs in the ab plane, and is slightly rotated about the c axis [27]. The Ir ions occupy the center of the square-planar coordination environment. The average distance of four Ir-O bonds in the square-planar IrO_4 is 1.91 Å, which is similar to the Ir-O bond length in the IrO_6 octahedron. Instead of the face-sharing (or edge- or corner-sharing) structure of octahedrons, the IrO_4 moiety is quite isolated as shown in Fig. 1, thus the Ir-Ir distance is very large. These remarkable structural features significantly affect the electronic structure and magnetic properties of Na_4IrO_4 as shown in the following sections.

III. BAND STRUCTURES

To clarify the basic electronic features, we perform nonmagnetic local-density approximation (LDA) calculation, and show the band structures and the DOS in Figs. 2(a) and 3, respectively. The high-symmetry k points used in band structures are shown in Fig. 1(c). The Ir 5*d* orbitals and corresponding partial densities are defined in the local coordinated frame, which is slightly rotated about the c axis from the global one. As shown in Fig. 3, O-2*p* states are mainly located between -7.0 and -1.5 eV. Na 3*s* and 3*p* bands, appearing mainly above 2.2 eV, have also considerable distribution between -7.0 and -1.5 eV, indicating the non-negligible hybridization between Na and O states despite the fact that Na is highly ionic. Hence the chemical valence for Na is $+1$ while that for O is -2. As a result, the nominal valence of Ir in Na_4IrO_4 is $+4$, and the electronic configuration of the Ir ion is $5d^5$. It is well known that in the octahedral environment the 5*d* orbitals will split into the t_{2g} and e_g states, and the strong SOC in 5*d* electrons splits the t_{2g} states into $J_{\text{eff}} = 1/2$ and $3/2$ bands [6,7]. Compared with the IrO_6 octahedra, the upper and lower O^{2-} ions are absent in the square-planar IrO_4 oxoanion. Consequently the Ir-5*d* orbitals split into three nondegenerate orbitals—$d_{3z^2-r^2}$, d_{xy}, and $d_{x^2-y^2}$—and doubly

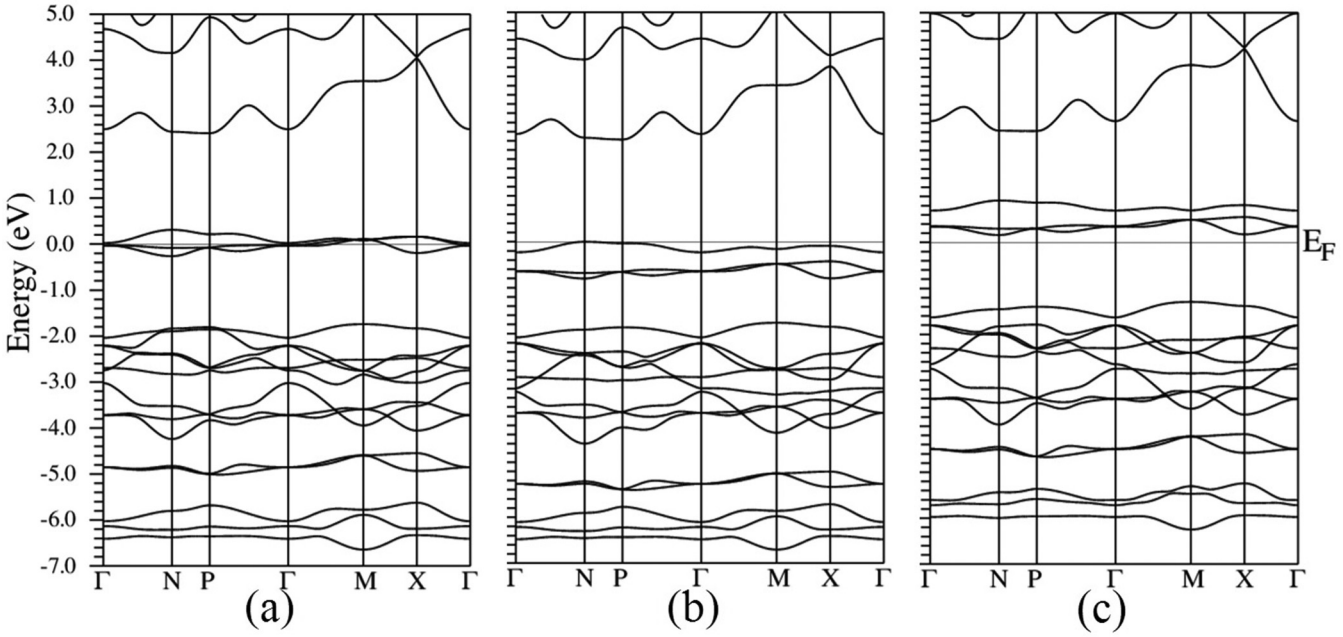

FIG. 2. Band structures of Na_4IrO_4. (a) LDA calculation. (b, c) Spin-up and spin-down channel, respectively, from LSDA calculation with FM configuration. The Fermi energy is set to zero.

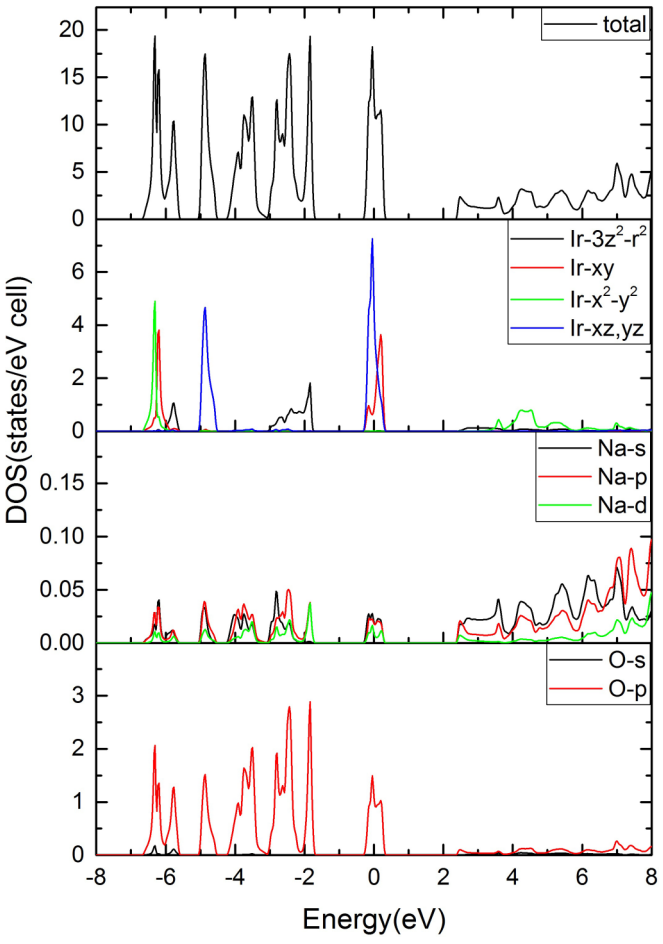

FIG. 3. Partial density of states of Na_4IrO_4 from LDA calculation. The Fermi energy is set to zero.

degenerate d_{xz}/d_{yz} ones. There are in total 13 bands in the energy range from −7.0 to −1.0 eV, as shown in Fig. 2(a). The $d_{3z^2-r^2}$ states appear mainly between −3.0 and −2.0 eV, while the remaining 12 bands are contributed by O-2p states. Mainly located above 4 eV, $d_{x^2-y^2}$ states have also large distribution around −6.5 eV due to the strong hybridization with O-2p bands. The d_{xz}/d_{yz} and d_{xy} orbitals are mainly located from −1.0 to 1.0 eV, while the d_{xy} state is slightly higher in energy. As shown in Figs. 2(a) and 3, these bands are separated from other bands, and around the Fermi level the orbital splitting can be displayed by the left panel of Fig. 6. The dispersion of the 5d bands around the Fermi level is very narrow, due to the fact that the IrO_4 moiety is quite isolated in the crystal structure. As shown in Fig. 3, the DOS at Fermi level is rather high, which indicates the magnetic instability.

To understand the magnetic properties, we also perform a spin-polarized calculation and show the band structures of ferromagnetic (FM) configuration in Figs. 2(b) and 2(c). Basically, the $d_{3z^2-r^2}$ states are fully occupied while the $d_{x^2-y^2}$ ones are empty, and the spin polarization has a relatively small effect on these bands. On the other hand, the partially occupied d_{xz}/d_{yz} and d_{xy} states are significantly affected, and these bands have about 1-eV exchange splitting, as shown in Figs. 2(b) and 2(c). LSDA calculation for FM configuration gives an insulating solution with a band gap of 0.16 eV. Experiment reveals that Na_4IrO_4 has a long-range antiferromagnetic (AFM) order at low temperature [28]. Thus we also explore the magnetic configuration. In addition to the FM configuration, we also consider three AFM states: AFM-1, where Ir atoms at the body center and corners have opposite spin orientations; AFM-2, where Ir atoms couple antiferromagnetically along the a axis; and AFM-3, where Ir atoms couple antiferromagnetically along the c axis (see Fig. 4 for the magnetic structures of different AFM configurations).

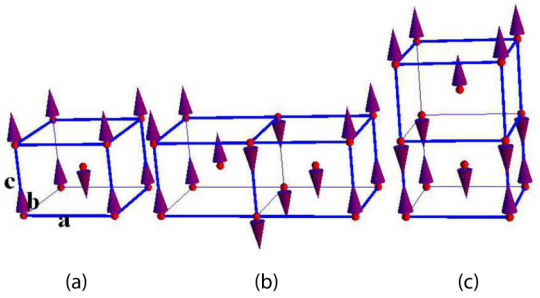

FIG. 4. The AFM magnetic configurations of Na_4IrO_4 which we considered in DFT calculations. For clarity only Ir atoms are shown. (a–c) AFM-1, AFM-2, and AFM-3 configurations, respectively.

The relative total energies and magnetic moments for the four magnetic configurations are summarized in Table I. Different magnetic configurations have similar calculated magnetic moments. This indicates that the magnetism in Na_4IrO_4 is quite localized. The distance between IrO_4 oxoanions is quite large as shown in Fig. 1, where the nearest-neighbor distance for Ir ions is 4.7 Å. Thus, the effective hopping between Ir ions in Na_4IrO_4 is very weak. As a result, the magnetism in Na_4IrO_4 is very localized and different magnetic configurations have only small effects on the band structures. Regardless of the magnetic configuration, our numerical results show that the $5d$ electronic configuration can always be described by $d^1_{3z^2-r^2,\uparrow} d^1_{3z^2-r^2,\downarrow} d^1_{xz,\uparrow} d^1_{yz,\uparrow} d^1_{xy,\uparrow}$, while for most of the $5d$ transition-metal oxides the magnetization is quite itinerant and the magnetic configuration strongly affects the band structure [5]. The calculated magnetic moment at the Ir site is around $1.35\mu_B$, considerably smaller than that of the $S = 3/2$ configuration. Due to the strong hybridization between Ir-$5d$ and O-$2p$ states, there is also considerable magnetic moment located at the O site. As shown in Table I, the AFM-1 configuration has the lowest total energy. Although we only consider four magnetic configurations, we believe that AFM-1 is indeed the magnetic ground-state configuration, as discussed in the following sections.

As the importance of electronic correlation for $5d$ orbitals has been recently emphasized [3–5], we utilize the LSDA + U scheme, which is adequate for the magnetically ordered insulating ground states, to consider the electronic correlation in Ir-$5d$ states. The estimates for the values of U have been recently obtained between 1.4 and 2.4 eV in layered Sr_2IrO_4 and Ba_2IrO_4 [39]. The Ir ion in the IrO_4 moiety has only four nearest neighbors. Moreover, IrO_4 moieties are highly isolated, thus we generally expect that the value of U in Na_4IrO_4 is larger than that in other $5d$ transition-metal oxides. We have varied the value of U from 2.0 to 4.0 eV, and the electronic structure and magnetic properties depend moderately on U. The numerical calculations show that with increasing U the total-energy differences among the FM and AFM configurations become smaller, but the AFM-1 state is always the ground state. The numerical results also show that the essential properties and our conclusions do not depend on the value of U. Thus, we only show the results with $U = 2$ eV in the following. Similarly we consider the four magnetic configurations (the results of relative total energies and magnetic moments are also summarized in Table I), while the AFM-1 state still has the lowest energy. The band structure of Na_4IrO_4 with AFM-1 order from the LSDA + U calculation is presented in Fig. 5. The result from the LSDA calculation within the AFM-1 configuration is also shown for comparison. Compared with the LSDA calculation, the bands within the LSDA + U scheme are narrower but the order of the crystal-field splitting pattern and electronic occupation does not change. Including U will enhance the exchange splitting in $5d$ bands, and slightly enlarge the calculated magnetic moments and band gap as shown in Table I and Fig. 5. We also show the d-orbital splitting under the crystal field of the square plane in the middle panel of Fig. 6, and the electronic occupation pattern is decided by the competition between the crystal-field splitting and Hund's rule. It is worth mentioning that results such as the crystal splitting pattern are not dependent on the value of U.

TABLE I. The calculated total energy (in meV) per unit cell and magnetic moments (in μ_B) for the four magnetic configurations from LSDA and LSDA +U ($U = 2$ eV) calculations. The total energy of the AFM1 state is set to zero.

	LSDA				LSDA+U			
	FM	AFM1	AFM2	AFM3	FM	AFM1	AFM2	AFM3
E_{total}	44.5	0	19.7	17.9	22.8	0	10.8	8.4
m_{Ir}	1.40	1.32	1.34	1.35	1.48	1.45	1.46	1.46
m_{O}	0.27	0.25	0.26	0.26	0.26	0.25	0.26	0.26

The strong SOC in $5d$ atoms usually significantly affects the band dispersions, thus we also perform the LSDA + U + SOC calculations. Since the IrO_4 moiety is in the ab plane, we perform the LSDA + U + SOC calculations with spin orientations perpendicular to the ab plane and lying in the ab plane, i.e., the spin orientations are along (001), (010), and (100) directions. Our calculations show that (001) is the easy axis and (100) is the hard axis. We list the calculated magnetic moments and total energies in Table II and find that the AFM-1 state is still the ground-state configuration. Unlike LSDA + U calculations, the degeneracy of d_{xz} and d_{yz} is removed by SOC, as shown in Fig. 7 and the right panel of Fig. 6. The most remarkable feature is the huge MAE. The MAE of Na_4IrO_4 is around 12 meV per Ir atom with the highly preferential easy axis being out of the ab plane. It is easy to see from Table II that for all of the four magnetic configurations the (001) direction is the easy axis and the MAEs have similar values from 11.6 to 12.6 meV per Ir atom.

In addition to calculating the MAE by energy differences approach, we also calculate the MAE by using the force theorem [40,41]. The MAE from force theorem calculation is about 12.9 meV for the AFM-1 configuration. This confirms the giant MAE in Na_4IrO_4. We try to understand the magnetic properties in the following sections.

IV. SPIN MODEL

As shown in Table I, the calculated magnetic moments for the different magnetic configurations are similar, thus the total-energy differences between the different magnetic configurations are mainly contributed by the interatomic

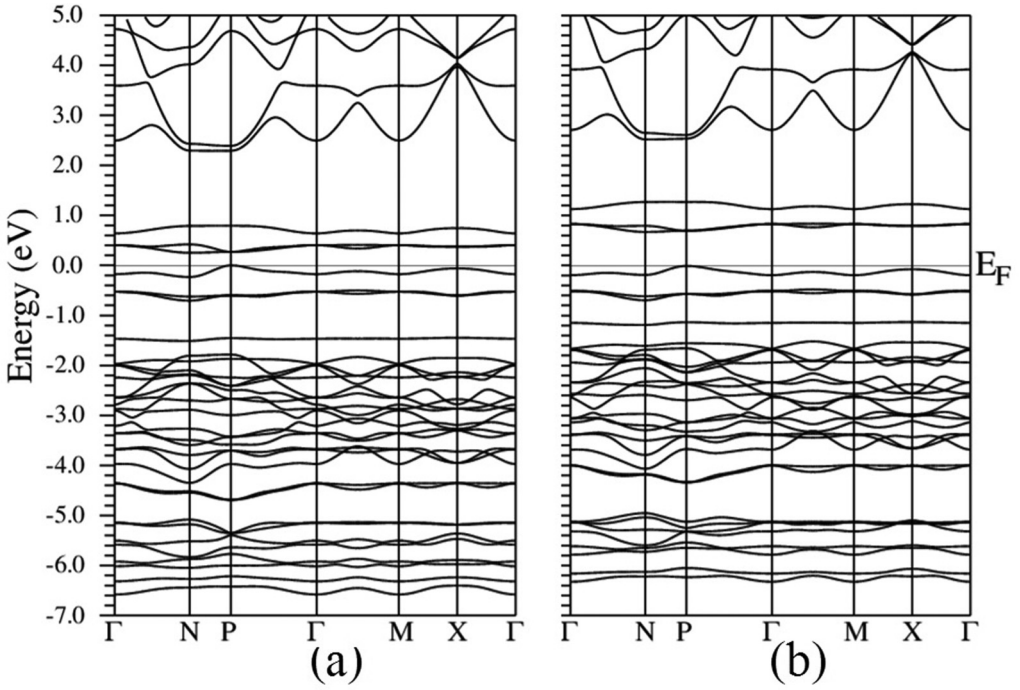

FIG. 5. Band structure of the AFM-1 configuration calculated by the (a) LSDA and (b) LSDA + U (= 2 eV) method.

exchange interaction where SOC is not considered. This allows us to estimate the exchange couplings by the energy-mapping analysis (see the Appendix). As shown in Fig. 1, we consider three spin-exchange paths. J_1 is the nearest-neighbor Ir-Ir exchange coupling along the c axis, J_2 is the next-nearest-neighbor one along the diagonal line, while J_3 is the third-nearest-neighbor one along the a/b axis. The distance in J_3 (7.1 Å) is much longer than J_1 (4.7 Å) and J_2 (5.6 Å). Compared with LSDA + U, LSDA overestimates the hopping and consequently gives larger exchange parameters as shown in Table III. J_1, J_2, and J_3 are all AFM. Although J_1 has the nearest-neighbor exchange path, the $d_{3z^2-r^2}$ orbital is fully occupied in both the up- and down-spin channel as mentioned in the previous section and the hoppings for the other d orbitals

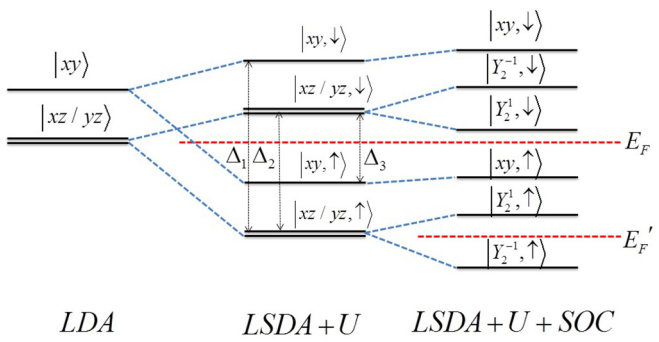

FIG. 6. Schematic picture of orbital occupation around Fermi level. From LDA (left panel), LSDA+U (middle panel), and LSDA+U+SOC (right panel) calculations. LSDA calculation has the same pattern with LSDA+U calculations and is not presented here. E_F represents the Fermi level of Na_4IrO_4. As discussed in the main text, substituting Ir ions by Re ions, the Fermi level shifts to E_F', which significantly enhances the MAE.

are relatively small. Therefore, it is easy to understand that the value of J_1 is less than J_2. Thus J_2 dominates over the others in strength, while J_3 is nearly negligible due to the very long distance, as shown in Table III. Although the spin-exchange couplings J_1-J_3 decrease with increasing U values, J_2 is always dominated while J_3 is nearly negligible. The exchange interaction in magnetic insulators is predominantly caused by the so-called superexchange—which is due to the overlap of the localized orbitals of the magnetic electrons with those of intermediate ligands—since the IrO_4 moieties are strongly localized and the exchange path of J_3 is already quite large (7.1 Å). Thus, the further exchange interaction J should be negligible and have no influence on the magnetic ground state, and we believe that the strongest J_2 makes AFM-1 the ground state in agreement with the total-energy calculations.

Based on the J_1-J_3 parameters from LSDA + U(U = 2 eV) calculations as shown in the second column in Table III, we

TABLE II. The calculated total energy (in meV) per unit cell and magnetic moments (in μ_B) for the four magnetic configurations from LSDA + SOC + U (U = 2 eV) calculations with (001) and (100) spin orientations. The total energy of the AFM-1 state with (001) magnetization direction is set to zero. MAE (in meV) per Ir atom for four magnetic configurations is also summarized in the table.

	FM		AFM-1		AFM-2		AFM-3	
	(001)	(100)	(001)	(100)	(001)	(100)	(001)	(100)
E_{total}	22.3	34.4	0	11.6	11.1	22.8	8.9	21.5
m_{Ir} (spin)	1.37	1.38	1.34	1.35	1.36	1.36	1.36	1.36
m_{Ir} (orbital)	0.11	0.10	0.10	0.10	0.10	0.10	0.10	0.10
m_O	0.25	0.24	0.24	0.23	0.24	0.24	0.24	0.24
MAE	12.1		11.6		11.7		12.6	

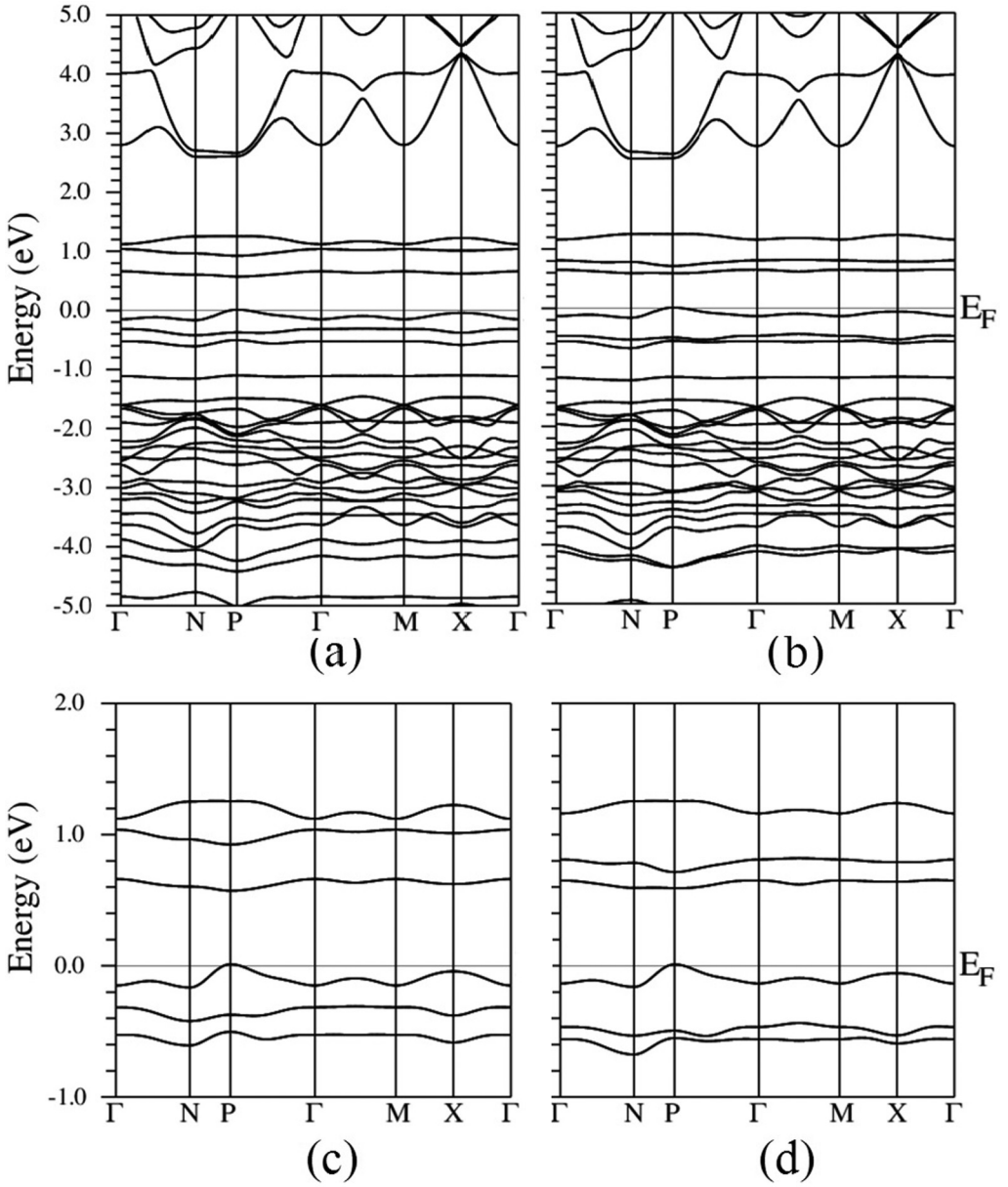

FIG. 7. Band structure of Na_4IrO_4 from LSDA + U + SOC (U = 2 eV) calculation. (a, b) Spin orientations along the (001) direction and (100) direction, respectively. (c, d) Band structures in a narrow energy range to illustrate the dispersion around the Fermi level clearly.

calculate the Curie-Weiss temperature θ and Néel temperature T_N using the mean-field approximation theory [42]. θ is estimated to be −105 K while T_N is about 56 K. The values of −105 and 56 K are both somewhat larger than the experimental ones of −78 and 25 K, respectively. Since the mean-field approximation theory often overestimates the Curie-Weiss and Néel temperatures, our mapping J_1-J_3 parameters are thought to be in reasonable agreement with experimental results.

TABLE III. Isotropic spin-exchange parameters (in meV) and anisotropic spin-exchange parameters evaluated by energy-mapping analysis from LSDA, LSDA + U, and LSDA + SOC + U (U = 2 eV) calculations, respectively.

			LSDA+U+SOC		
	LSDA	LSDA+U	J_i^{xx}	J_i^{yy}	J_i^{zz}
J_1/meV	0.97	0.66	0.32	0.32	0.51
J_2/meV	2.47	1.27	1.21	1.35	1.24
J_3/meV	0.56	0.14	0.02	0.02	0.01
K/meV				5.4	

V. MAGNETIC ANISOTROPY ENERGY

In order to understand the origin of the giant MAE, we start from a generalized symmetry allowed spin model of Na_4IrO_4 (see the Appendix):

$$H_S = -K\sum_i S_i^{z2} + \frac{1}{2}\sum_{<i,j>,\alpha\beta} J_{ij}^{\alpha\beta} S_i^{\alpha} S_j^{\beta}, \qquad (1)$$

where the first term represents the single-ion anisotropy Hamiltonian, the second one represents the interatomic

exchange Hamiltonian, i and j label the Ir ions, and the α and β represent the Cartesian coordinates x, y, and z. Due to the inversion symmetry, $J_{ij}^{\alpha\beta} = J_{ij}^{\beta\alpha}$, which means there is no Dzyaloshinskii-Moriya interaction [43,44]. We only consider the exchange neighbors $< ij >' s$ to the third-nearest neighbor, which are denoted by J_1, J_2, and J_3 in order as shown in Fig. 1. For J_1, due to the C_4 rotation symmetry, $J_1^{\alpha\beta} = \delta_{\alpha\beta} J_1^{\alpha\alpha}$ and $J_1^{xx} = J_1^{yy}$, while for J_2 and J_3 the nondiagonal terms (i.e., J^{xy}, J^{yz}, and J^{zx}) are symmetry allowed; however, these terms are proportional to the product of λ^2 and isotropic exchange [45] and should be very small, thus we ignore them hereafter.

Using a similar energy-mapping method (see the Appendix), we estimate the parameters in Eq. (1) and show the results in Table III. It is clear that the anisotropy of spin exchange is small, especially for the dominating spin exchange, where J_2 shows a small difference between J_2^{xx}, J_2^{yy}, and J_2^{zz}. The different spin configurations have almost the same value of MAE as shown in Table II, and the anisotropy of spin-exchange coupling parameters is little, indicating that MAE is dominated by the single-ion anisotropy.

To understand the origin of single-ion anisotropy, we consider the crystal-field splitting, the electronic occupation shown in the middle panel of Fig. 6, and the SOC Hamiltonian λLS where λ is the SOC constant. With the spin direction described by the two angles θ and φ, the azimuthal and polar angles of the spin orientation with respect to the local coordinate environment, the λLS term can be written as [46]

$$H_{\mathrm{SO}} = \lambda \hat{S}_{z'}\left(\hat{L}_z \cos\theta + \frac{1}{2}\hat{L}_+ e^{-i\varphi}\sin\theta + \frac{1}{2}\hat{L}_- e^{i\varphi}\sin\theta\right) + \frac{\lambda}{2}\hat{S}_{+'}\left(-\hat{L}_z \sin\theta - \hat{L}_+ e^{-i\varphi}\sin^2\frac{\theta}{2} + \hat{L}_- e^{i\varphi}\cos^2\frac{\theta}{2}\right)$$
$$+ \frac{\lambda}{2}\hat{S}_{-'}\left(-\hat{L}_z \sin\theta + \hat{L}_+ e^{-i\varphi}\cos^2\frac{\theta}{2} + \hat{L}_- e^{i\varphi}\sin^2\frac{\theta}{2}\right). \quad (2)$$

Using perturbation theory by treating the SOC Hamiltonian as the perturbation combined with the d-orbital occupation pattern, we can get the associated energy lowering:

$$\Delta E^{(1)} = \sum_i \langle i|H_{\mathrm{SO}}|i\rangle, \quad \Delta E^{(2)} = -\sum_{i,j}\frac{|\langle i|H_{\mathrm{SO}}|j\rangle|^2}{|e_i - e_j|} \quad (3)$$

where i represents an occupied d-level state with energy e_i while j represents an unoccupied d-level state with energy e_j, and the third- and higher-order perturbations are not given here. In Na_4IrO_4, where the SOC has not been considered, $d_{xz,\uparrow}$ and $d_{yz,\uparrow}$ are doubly degenerate. We can see that the degeneracy of $d_{xz,\uparrow}$ and $d_{yz,\uparrow}$ is lifted by the SOC and they split to $|Y_2^1, \uparrow\rangle$ and $|Y_2^{-1}, \uparrow\rangle$. The splitting is $\pm\frac{\lambda}{2}|\cos\theta|$ according to the first-order perturbation, thus the splitting for the spin polarization of the (001) direction is larger than that for the (100) direction, as shown in Fig. 7. However, $d_{xy,\uparrow}$, $d_{xz,\uparrow}$, and $d_{yz,\uparrow}$ are fully occupied and the band gap is quite big with respect to the SOC constant λ. SOC does not change the $d_{xy,\uparrow}$ state much. Considering the electronic occupation, the first-order perturbation has negligible effect on total energy and the single-ion anisotropy.

Therefore, we consider the second-order perturbation. Note that in the common $5d$ transition-metal oxides with face-sharing (or edge- or corner-sharing) structure of oxygen octahedrons, the widths of the t_{2g}-block bandwidths are relatively large while the $|e_i - e_j|$ values are relatively small, so the perturbation theory does not lead to an accurate estimation of MAE. But in Na_4IrO_4, the widths of the bands around the Fermi level are about 0.2 eV and the $|e_i - e_j|$ value is around $\sim$2 eV, thus one can get the quantitative value of MAE more accurately by the second-order perturbation:

$$E = -\lambda^2 \cos^2\theta\left[\frac{1}{4\Delta_1} + \frac{1}{4\Delta_3} - \frac{1}{2\Delta_2}\right]. \quad (4)$$

Here Δ_i is the splitting of on-site d-orbital energy levels, as shown in the middle panel of Fig. 6. The orbitals of $d_{x^2-y^2}$ and d_{z^2} are far away from the Fermi level and can be ignored. From the LSDA + U (U = 2 eV) calculations, we estimate the orbital energy levels by the weight-center positions of the DOS and get the values of Δ_i. The calculated values of Δ_1, Δ_2, and Δ_3 are 1.82, 1.35, and 0.89 eV, respectively. Using these values of Δ_i and $\lambda = 0.5$ eV, we get the MAE as 12.0 meV, consistent with the value directly from DFT calculations. Thus the second-order perturbation is dominant in MAE and higher-order perturbations are believed to be little. One reason for the giant MAE is the SOC strength, which is very strong for $5d$ electrons. It is about three times as high as $4d$ electrons and an order of magnitude higher than $3d$ electrons. Besides the strong SOC strength, the d-level splitting is also an important cause of the giant MAE. The d-level splitting

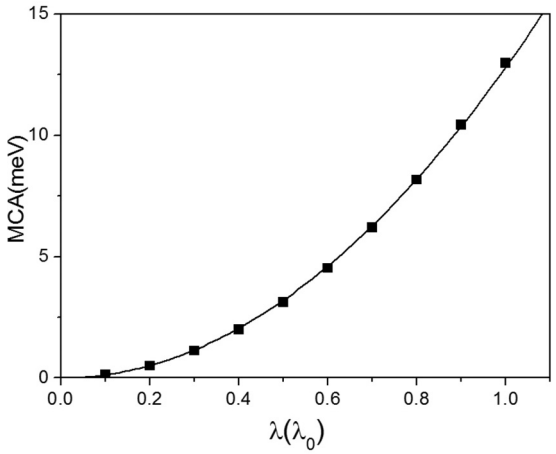

FIG. 8. The MAE of Na_4IrO_4 as a function of the SOC strength λ. The calculation is done by LSDA + U + SOC (U = 2 eV).

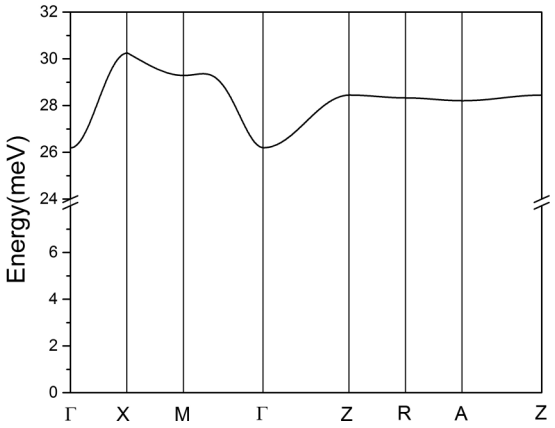

FIG. 9. Calculated spin-wave dispersion curves along the high-symmetry axis for Na_4IrO_4.

condition comes from the low-symmetry square-planar local environment, which indicates a giant anisotropy between in-plane and out-of-plane orientations. The long distances of IrO_4 moieties make the strongly localized magnetization. These factors together make the giant value of MAE.

We also calculate MAE with varying the SOC strength λ within the LSDA + U + SOC scheme. As shown in Fig. 8, it is obvious that the MAE of Na_4IrO_4 is nearly proportional to the square of λ, in accordance with the second-order perturbation term of Eq. (4).

Using the calculated spin model parameters, one can obtain the magnon spectrum on the basis of the Holstein-Primakoff transformation and the Fourier transformation. The spin-wave dispersion can be written as

$$E(\vec{q}) = \sqrt{A(\vec{q})^2 - B(\vec{q})^2} \tag{5}$$

where $\vec{q}$ is the magnon wave vector,

$$A(\vec{q}) = S\Big[\sum_{i,j} J_{ij}^{yy}\cos(\vec{q}\cdot\vec{r_{ij}}) - 2\sum_{i,j} J_{ij}^{zz}\cos(\vec{Q}\cdot\vec{r_{ij}}) + \sum_{i,j} J_{ij}^{xx}\cos(\vec{Q}\cdot\vec{r_{ij}})\cos(\vec{q}\cdot\vec{r_{ij}}) + 2K\Big], \tag{6}$$

$$B(\vec{q}) = S\Big[\sum_{i,j} J_{ij}^{yy}\cos(\vec{q}\cdot\vec{r_{ij}}) - \sum_{i,j} J_{ij}^{xx}\cos(\vec{Q}\cdot\vec{r_{ij}}) \times \cos(\vec{q}\cdot\vec{r_{ij}})\Big]. \tag{7}$$

Here $\vec{r_{ij}}$ is the relative position of Ir atoms and $\vec{Q}$ is $(0,0,2\pi)$. We show the spin-wave dispersion along the high-symmetry axis in Fig. 9. As shown in Fig. 9, there is a large spin gap of about 26 meV while the width of spin-wave dispersion is only 4 meV. This is due to the large single-ion anisotropy and relatively small interatomic exchange couplings.

VI. MATERIAL DESIGN

As shown in Fig. 6, for Na_4IrO_4, the exchange splitting is large and there is a relatively big gap between occupied and unoccupied states. Therefore the first-order perturbation has small influence on total energy. We expect that if the Fermi level shifts to the position of E_F' as shown in the right panel of Fig. 6, there is considerable first-order energy correction and the MAE will be enhanced significantly. We try to realize this Fermi-level shift through substituting Ir ions in Na_4IrO_4 by Re ions. The MAE of Na_4ReO_4 may be even larger and it may reach the limit of MAE even in bulk materials, with the same size as Co or other atoms absorbed on top of the O sites of the MgO (001) surface [47,48].

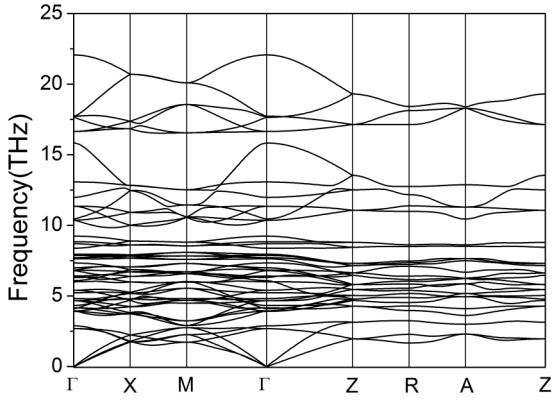

FIG. 10. Calculated phonon dispersion for Na_4ReO_4.

In order to examine the dynamic stability, we calculate the phonon spectrum of Na_4ReO_4 (see the Appendix), and show the calculated phonon spectrum along high-symmetry lines in Fig. 10. All the phonon modes of Na_4ReO_4 are positive, indicating the structure is dynamically stable.

The calculated value of MAE is about 140 meV per Re atom. It can be explained by the same method using perturbation theory, where Na_4ReO_4 has two less occupied electrons. For Na_4ReO_4, with the absence of SOC interaction, the orbitals of $d_{xz,\uparrow}$ and $d_{yz,\uparrow}$ are doubly degenerate and half occupied. With the presence of SOC, the doubly degenerate $d_{xz,\uparrow}$ and $d_{yz,\uparrow}$ bands split to $|Y_2^1, \uparrow\rangle$ and $|Y_2^{-1}, \uparrow\rangle$, where $|Y_2^{-1}, \uparrow\rangle$ is fully occupied while $|Y_2^1, \uparrow\rangle$ is fully unoccupied. Thus the first-order perturbation of total energy can be written as

$$E = -\frac{\lambda}{2}|\cos\theta|. \tag{8}$$

The calculated MAE of 140 meV is in good agreement with the expected value of $\frac{\lambda}{2}$, as the SOC strength λ of the 5d electrons is generally regarded as 0.3–0.5 eV.

VII. CONCLUSIONS

In conclusion, using first-principles calculation and perturbation theory, we present a comprehensive investigation of the 5d transition-metal oxides Na_4IrO_4, where Ir occupies the center of the square-planar coordination environment. We discuss its electronic structures, determine its magnetic ground-state configuration, and find a giant MAE for this compound. Its spin-wave spectrum is characterized by a large spin gap and quite narrow dispersion. We discuss the origin of these novel magnetic properties, and also suggest a possible way to further enhance MAE. We expect that the 5d transition-metal oxides with low symmetry and long 5d-5d distance may exhibit giant MAE and extraordinarily

large coercive fields. The prediction about giant MAE calls for experimental tests and may provide a route to nanoscale magnetic devices.

Note added. After submission of this paper we became aware of a theoretical study of Na_4IrO_4 by Ming *et al.* [49]. They have also calculated MAE in Na_4IrO_4 and found a similarly large anisotropy.

ACKNOWLEDGMENTS

This work was supported by the National Key Research and Development Program of China (Grant No. 2017YFA0303203), the National Natural Science Foundation of China (Grants No. 11525417 and No. 11374137), and the Natural Science Foundation of Jiangsu Province (Grant No. BK20170821).

APPENDIX

1. Symmetry analysis

Symmetry will add restrictions on the magnetic model. To the quadratic terms of spins, the magnetic model can be written in the following general form:

$$H = \frac{1}{2}\sum_{ls,l's'} S_{ls}^{\dagger} J(ls,l's') S_{l's'}, \tag{A1}$$

where S_{ls} represents the magnetic moment located at the magnetic ion labeled by s in the lth unit cell. $J(ls,l's')$ is the exchange interaction between S_{ls} and $S_{l's'}$. It is obviously a 3×3 real matrix, because the magnetic moment is a three-component vector. We adopt the conventional Cartesian coordinate system. Translation symmetry will restrict $J(ls,l's')$ to be only related to $l'-l$, irrespective of the starting unit cell. Rotation, inversion, or the combination of the two will also give restrictions on the exchange matrix. Consider a general space-group element, $\{\alpha|\mathbf{t}\}$, of which α is the Point-group operation. We can get the representation matrix of α in the coordinate system here, which is denoted by $R(\alpha)$. Then $J(ls,l's')$ should satisfy that

$$R(\alpha)^{\dagger} J(mp,m'p') R(\alpha) = J(ls,l's'), \tag{A2}$$

where mp and $m'p'$ are related to ls and $l's'$ by the action of $\{\alpha|\mathbf{t}\}$, respectively.

We then get ready to turn to the symmetry allowed magnetic model for Na_4IrO_4. Because there is only one magnetic ion, namely, Ir, in one unit cell, we can just label the magnetic moment by the unit-cell label l. Utilizing the translation property, we just need to consider $J(0,l)$, which we denote to be $J(l)$ or $J(l_1,l_2,l_3)$ hereafter. The onsite exchange $J(0,0,0)$ is found to have the following form:

$$J(0,0,0) = \begin{pmatrix} J(0,0,0)_{11} & 0 & 0 \\ 0 & J(0,0,0)_{11} & 0 \\ 0 & 0 & J(0,0,0)_{33} \end{pmatrix}, \tag{A3}$$

which represents the first term of Eq. (1) as the single-ion anisotropy $\sim S_z^2$.

According to the crystal structure, we find that $l=(0,0,1)$ and $(0,0,-1)$ for the nearest neighborhoods, $l=(\eta_1 1/2,\eta_2 1/2,\eta_3 1/2)(\eta_i=\pm)$ for the eight next-nearest neighborhoods, and $l=(\pm 1,0,0),(0,\pm 1,0)$ for the third-nearest neighborhoods.

Then $J(0,0,\pm 1)$ are found to be in the following form:

$$J(0,0,\pm 1) = \begin{pmatrix} J(0,0,1)_{11} & 0 & 0 \\ 0 & J(0,0,1)_{11} & 0 \\ 0 & 0 & J(0,0,1)_{33} \end{pmatrix}, \tag{A4}$$

and note that in the main text we relabel $J(0,0,1)_{11}$ and $J(0,0,1)_{33}$ to be J_1^{xx} and J_1^{zz}, respectively.

For the next-nearest neighborhoods, inversion symmetry will restrict $J(1/2,1/2,1/2)$ to be a symmetric matrix. However, no symmetries will restrict the nondiagonal elements of $J(1/2,1/2,1/2)$ to be vanishing. We will ignore these symmetric nondiagonal elements, because physically they are relatively small [45]. Then the $J(\eta_1 1/2,\eta_2 1/2,\eta_3 1/2)$ are in the following form:

$$J(\eta_1 1/2,\eta_1 1/2,\pm 1/2) = \begin{pmatrix} J(1/2,1/2,1/2)_{11} & 0 & 0 \\ 0 & J(1/2,1/2,1/2)_{22} & 0 \\ 0 & 0 & J(1/2,1/2,1/2)_{33} \end{pmatrix}, \tag{A5}$$

$$J(\eta_1 1/2,-\eta_1 1/2,\pm 1/2) = \begin{pmatrix} J(1/2,1/2,1/2)_{22} & 0 & 0 \\ 0 & J(1/2,1/2,1/2)_{11} & 0 \\ 0 & 0 & J(1/2,1/2,1/2)_{33} \end{pmatrix}, \tag{A6}$$

and note that in the main text we relabel $J(1/2,1/2,1/2)_{11}$, $J(1/2,1/2,1/2)_{22}$, and $J(1/2,1/2,1/2)_{33}$ to be J_2^{xx}, J_2^{yy}, and J_2^{zz}, respectively.

Finally $J(\pm 1,0,0)$ and $J(0,\pm 1,0)$ are found to be in the following form:

$$J(\pm 1,0,0) = \begin{pmatrix} J(1,0,0)_{11} & J(1,0,0)_{12} & 0 \\ J(1,0,0)_{12} & J(1,0,0)_{22} & 0 \\ 0 & 0 & J(1,0,0)_{33} \end{pmatrix}, \tag{A7}$$

$$J(0,\pm 1,0) = \begin{pmatrix} J(1,0,0)_{22} & -J(1,0,0)_{12} & 0 \\ -J(1,0,0)_{12} & J(1,0,0)_{11} & 0 \\ 0 & 0 & J(1,0,0)_{33} \end{pmatrix}, \tag{A8}$$

and note that in the main text we relabel $J(1,0,0)_{11}$, $J(1,0,0)_{22}$, and $J(1,0,0)_{33}$ to be J_3^{xx}, J_3^{yy}, and J_3^{zz}, respectively. The nondiagonal elements $J(1,0,0)_{12}$ are still thought to be very small and ignored [45].

2. Energy-mapping analysis

We evaluate spin-exchange parameters J_1-J_3 by energy-mapping analysis. First we consider four magnetic configurations as shown in Fig. 4. The total energies of these four magnetic states can be described in terms of the spin Hamiltonian:

$$H = \sum_{i<j} J_{ij} \hat{S}_i \cdot \hat{S}_j \tag{A9}$$

where J_{ij} (= J_1, J_2, J_3) is the interatomic exchange parameter between the spin sites i and j. By applying the energy expressions obtained for a spin dimer of Ir^{4+} ions, the total energies per unit cell for these four spin configurations are expressed as

$$E_{\mathrm{FM}} = (2J_1 + 8J_2 + 4J_3)\left(\frac{S^2}{2}\right), \tag{A10}$$

$$E_{\mathrm{AFM1}} = (2J_1 - 8J_2 + 4J_3)\left(\frac{S^2}{2}\right), \tag{A11}$$

$$E_{\mathrm{AFM2}} = 2J_1 \times \left(\frac{S^2}{2}\right), \tag{A12}$$

$$E_{\mathrm{AFM3}} = (-2J_1 + 4J_3)\left(\frac{S^2}{2}\right). \tag{A13}$$

The calculated magnetic moments for the four magnetic configurations have little difference, as shown in Table I. Thus, the values of J_1 to J_3 can be evaluated by mapping relative total energies of the four spin states, which are obtained from LSDA and LSDA + U (U = 2 eV) calculations. The calculated spin-exchange coupling parameters J_1 to J_3 are summarized in Table III. The spin exchanges J_1, J_2, and J_3 are all AFM and J_2 dominates over others in strength, while J_3 is almost negligible.

Considering a generalized symmetry allowed spin model described in Eq. (1), which includes the anisotropic part of J and single-ion anisotropy, the values of J^{xx}, J^{yy}, J^{zz}, and K can be determined by energy-mapping analysis of LSDA + U + SOC calculations with different magnetization directions. In order to estimate these values, one more magnetic configuration should be considered, as shown in Fig. 11. The total energies per unit cell with different magnetic configurations are expressed as

$$E_{\mathrm{FM}}^{(001)} = \left(2J_1^{zz} + 8J_2^{zz} + 4J_3^{zz}\right)\left(\frac{S^2}{2}\right) - KS^2, \tag{A14}$$

$$E_{\mathrm{AFM1}}^{(001)} = \left(2J_1^{zz} - 8J_2^{zz} + 4J_3^{zz}\right)\left(\frac{S^2}{2}\right) - KS^2, \tag{A15}$$

$$E_{\mathrm{AFM2}}^{(001)} = 2J_1^{zz} \times \left(\frac{S^2}{2}\right) - KS^2, \tag{A16}$$

$$E_{\mathrm{AFM3}}^{(001)} = \left(-2J_1^{zz} + 4J_3^{zz}\right)\left(\frac{S^2}{2}\right) - KS^2, \tag{A17}$$

$$E_{\mathrm{AFM4}}^{(001)} = \left(2J_1^{zz} - 4J_3^{zz}\right)\left(\frac{S^2}{2}\right) - KS^2, \tag{A18}$$

$$E_{\mathrm{FM}}^{(100)} = \left(2J_1^{xx} + 4J_2^{xx} + 4J_2^{yy} + 2J_3^{xx} + 2J_3^{yy}\right)\left(\frac{S^2}{2}\right), \tag{A19}$$

$$E_{\mathrm{AFM1}}^{(100)} = \left(2J_1^{xx} - 4J_2^{xx} - 4J_2^{yy} + 2J_3^{xx} + 2J_3^{yy}\right)\left(\frac{S^2}{2}\right), \tag{A20}$$

$$E_{\mathrm{AFM2}}^{(100)} = \left(2J_1^{xx} + 2J_3^{xx} - 2J_3^{yy}\right)\left(\frac{S^2}{2}\right), \tag{A21}$$

$$E_{\mathrm{AFM3}}^{(100)} = \left(-2J_1^{xx} + 2J_3^{xx} + 2J_3^{yy}\right)\left(\frac{S^2}{2}\right), \tag{A22}$$

$$E_{\mathrm{AFM4}}^{(100)} = \left(2J_1^{xx} - 4J_2^{xx} + 4J_2^{yy} - 2J_3^{xx} - 2J_3^{yy}\right)\left(\frac{S^2}{2}\right), \tag{A23}$$

$$E_{\mathrm{FM}}^{(010)} = \left(2J_1^{xx} + 4J_2^{xx} + 4J_2^{yy} + 2J_3^{xx} + 2J_3^{yy}\right)\left(\frac{S^2}{2}\right), \tag{A24}$$

$$E_{\mathrm{AFM1}}^{(010)} = \left(2J_1^{xx} - 4J_2^{xx} - 4J_2^{yy} + 2J_3^{xx} + 2J_3^{yy}\right)\left(\frac{S^2}{2}\right), \tag{A25}$$

$$E_{\mathrm{AFM2}}^{(010)} = \left(2J_1^{xx} - 2J_3^{xx} + 2J_3^{yy}\right)\left(\frac{S^2}{2}\right), \tag{A26}$$

$$E_{\mathrm{AFM3}}^{(010)} = \left(-2J_1^{xx} + 2J_3^{xx} + 2J_3^{yy}\right)\left(\frac{S^2}{2}\right), \tag{A27}$$

$$E_{\mathrm{AFM4}}^{(010)} = \left(2J_1^{xx} + 4J_2^{xx} - 4J_2^{yy} - 2J_3^{xx} - 2J_3^{yy}\right)\left(\frac{S^2}{2}\right). \tag{A28}$$

The relative total energies of these magnetic states are obtained from LSDA + U + SOC calculations, which are

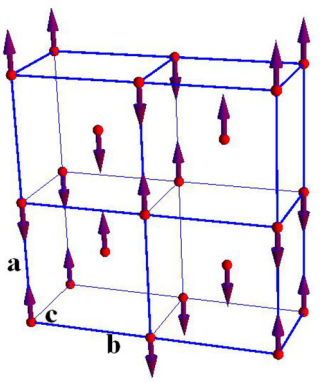

FIG. 11. The AFM-4 magnetic configuration of Na_4IrO_4. For clarity only Ir atoms are shown.

TABLE IV. The calculated total energy (in meV) per unit cell and magnetic moments (in μ_B) for the four magnetic configurations from LSDA + SOC + U ($U = 2$ eV) calculations with (001), (010), and (100) spin orientations for energy-mapping analysis.

	FM			AFM-1			AFM-2			AFM-3			AFM-4		
	(001)	(100)	(010)	(001)	(100)	(010)	(001)	(100)	(010)	(001)	(100)	(010)	(001)	(100)	(010)
E_{total}	22.3	34.4	34.4	0	11.6	11.6	11.1	22.8	22.8	8.9	21.5	21.5	10.9	23.3	21.7
m_{Ir} (spin)	1.37	1.38	1.38	1.34	1.35	1.35	1.36	1.36	1.36	1.36	1.36	1.36	1.36	1.36	1.36
m_{Ir} (orbital)	0.11	0.10	0.10	0.10	0.10	0.10	0.10	0.10	0.10	0.10	0.10	0.10	0.10	0.10	0.10
m_O	0.25	0.24	0.24	0.24	0.23	0.23	0.24	0.24	0.24	0.24	0.24	0.24	0.24	0.24	0.24

summarized in Table IV. The calculated magnetic moments for these magnetic configurations have little difference, as also summarized in Table IV. By energy-mapping analysis, the calculated anisotropic spin-exchange coupling parameters $J_i^{\alpha\alpha}$ and single-ion anisotropy parameter K are summarized in Table III.

3. Details of results for Na_4ReO_4

The phonon calculation is performed from the finite displacement method as implemented in the Vienna *ab initio* simulation package [50–52] and the PHONOPY package [53]. After a series of tests, a $3 \times 3 \times 2$ supercell is constructed to ensure the force convergence, and a $2 \times 2 \times 4$ k mesh for the Brillouin-zone sampling is used in the phonon calculation. The calculated phonon spectrum along high-symmetry lines is shown in Fig. 10.

In the Na_4ReO_4 case, the Re^{4+} ion has two less occupied $5d$ electrons than the Ir^{4+} ion. We perform first-principles calculations within the LSDA + U + SOC($U = 2$ eV) scheme and find that the crystal-field splitting does not change. The calculated magnetic moment is $0.51\mu_B$. We perform several calculations for different magnetic configurations and find that the magnetic ground-state configuration is the FM state. The calculated spin-exchange coupling parameters J_1 to J_3 are -1.84, -0.84, and -0.04 meV, respectively. However, the single-ion anisotropy has an overwhelmingly major contribution on MAE especially in Na_4ReO_4, which has an order-of-magnitude larger single-ion anisotropy than Na_4IrO_4 as shown in the main text.

[1] M. Imada, A. Fujimori, and Y. Tokura, Rev. Mod. Phys. **70**, 1039 (1998).

[2] G. Kotliar, S. Y. Savrasov, K. Haule, V. S. Oudovenko, O. Parcollet, and C. A. Marianetti, Rev. Mod. Phys. **78**, 865 (2006).

[3] W. Witczak-Krempa, G. Chen, Y. B. Kim, and L. Balents, Annu. Rev. Condens. Matter Phys. **5**, 57 (2013).

[4] J. G. Rau, E. K.-H. Lee, and H.-Y. Kee, Annu. Rev. Condens. Matter Phys. **7**, 195 (2016).

[5] Y. Du and X. Wan, Comput. Mater. Sci. **112**, 416 (2016).

[6] B. J. Kim, H. Jin, S. J. Moon, J.-Y. Kim, B.-G. Park, C. S. Leem, J. Yu, T. W. Noh, C. Kim, S.-J. Oh, J.-H. Park, V. Durairaj, G. Cao, and E. Rotenberg, Phys. Rev. Lett. **101**, 076402 (2008); B. J. Kim, H. Ohsumi, T. Komesu, S. Sakai, T. Morita, H. Takagi, and T. Arima, Science **323**, 1329 (2009).

[7] H. Jin, H. Jeong, T. Ozaki, and J. Yu, Phys. Rev. B **80**, 075112 (2009).

[8] H. Watanabe, T. Shirakawa, and S. Yunoki, Phys. Rev. Lett. **105**, 216410 (2010).

[9] A. Shitade, H. Katsura, J. Kuneš, X.-L. Qi, S.-C. Zhang, and N. Nagaosa, Phys. Rev. Lett. **102**, 256403 (2009).

[10] D. A. Pesin and L. Balents, Nat. Phys. **6**, 376 (2010).

[11] C. H. Kim, H. S. Kim, H. Jeong, H. Jin, and J. Yu, Phys. Rev. Lett. **108**, 106401 (2012).

[12] G. Jackeli and G. Khaliullin, Phys. Rev. Lett. **102**, 017205 (2009); J. Chaloupka, G. Jackeli, and G. Khaliullin, *ibid.* **105**, 027204 (2010).

[13] X. Wan, A. M. Turner, A. Vishwanath, and S. Y. Savrasov, Phys. Rev. B **83**, 205101 (2011).

[14] F. Wang and T. Senthil, Phys. Rev. Lett. **106**, 136402 (2011).

[15] Y. J. Yan, M. Q. Ren, H. C. Xu, B. P. Xie, R. Tao, H. Y. Choi, N. Lee, Y. J. Choi, T. Zhang, and D. L. Feng, Phys. Rev. X **5**, 041018 (2015).

[16] Y. K. Kim, N. H. Sung, J. D. Denlinger, and B. J. Kim, Nat. Phys. **12**, 37 (2015).

[17] X. Wan, A. Vishwanath, and S. Y. Savrasov, Phys. Rev. Lett. **108**, 146601 (2012).

[18] Y. Okamoto, M. Nohara, H. Aruga-Katori, and H. Takagi, Phys. Rev. Lett. **99**, 137207 (2007).

[19] P. A. Lee, Science **321**, 1306 (2008); L. Balents, Nature (London) **464**, 199 (2010).

[20] D. Mandrus, J. R. Thompson, R. Gaal, L. Forro, J. C. Bryan, B. C. Chakoumakos, L. M. Woods, B. C. Sales, R. S. Fishman, and V. Keppens, Phys. Rev. B **63**, 195104 (2001); W. J. Padilla, D. Mandrus, and D. N. Basov, *ibid.* **66**, 035120 (2002).

[21] Y. Shi, Y. Guo, X. Wang, A. J. Princep, D. Khalyavin, P. Manuel, Y. Michiue, A. Sato, K. Tsuda, S. Yu, M. Arai, Y. Shirako, M. Akaogi, N. Wang, K. Yamaura, and A. T. Boothroyd, Nat. Mat. **12**, 1024 (2013).

[22] H. Sim and B. G. Kim, Phys. Rev. B **89**, 201107(R) (2014); H. J. Xiang, *ibid.* **90**, 094108 (2014); H. M. Liu, Y. P. Du, Y. L. Xie, J.-M. Liu, C.-G. Duan, and X. Wan, *ibid.* **91**, 064104 (2015).

[23] Y. G. Shi, Y. F. Guo, S. Yu, M. Arai, A. A. Belik, A. Sato, K. Yamaura, E. Takayama-Muromachi, H. F. Tian, H. X. Yang, J. Q. Li, T. Varga, J. F. Mitchell, and S. Okamoto, Phys. Rev. B **80**, 161104 (2009).

[24] Y. Du, X. Wan, L. Sheng, J. Dong, and S. Y. Savrasov, Phys. Rev. B **85**, 174424 (2012); M.-C. Jung, Y.-J. Song, K.-W. Lee, and W. E. Pickett, *ibid.* **87**, 115119 (2013).

[25] B. Kim, P. Liu, Z. Ergönenc, A. Toschi, S. Khmelevskyi, and C. Franchini, Phys. Rev. B **94**, 241113(R) (2016).
[26] J. G. Vale, S. Calder, C. Donnerer, D. Pincini, Y. G. Shi, Y. Tsujimoto, K. Yamaura, M. Moretti Sala, J. van den Brink, A. D. Christianson, and D. F. McMorrow, arXiv:1707.05551 (2017).
[27] K. Mader and R. Hoppe, Z. Anorg. Allg. Chem. **619**, 1647 (1993).
[28] S. Kanungo, B. Yan, P. Merz, C. Felser, and M. Jansen, Angew. Chem. **127**, 5507 (2015).
[29] P. Gambardella, S. Rusponi, M. Veronese, S. S. Dhesi, C. Grazioli, A. Dallmeyer, I. Cabria, R. Zeller, P. H. Dederichs, K. Kern, C. Carbone, and H. Brune, Science **300**, 1130 (2003).
[30] C. F. Hirjibehedin, C. Y. Lin, A. F. Otte, M. Ternes, C. P. Lutz, B. A. Jones, and A. J. Heinrich, Science **317**, 1199 (2007).
[31] P. Blonski, A. Lehnert, S. Dennler, S. Rusponi, M. Etzkorn, G. Moulas, P. Bencok, P. Gambardella, H. Brune, and J. Hafner, Phys. Rev. B **81**, 104426 (2010).
[32] I. G. Rau, S. Baumann, S. Rusponi, F. Donati, S. Stepanow, L. Gragnaniello, J. Dreiser, C. Piamonteze, F. Nolting, S. Gangopadhyay, O. R. Albertini, R. M. Macfarlane, C. P. Lutz, B. A. Jones, P. Gambardella, A. J. Heinrich, and H. Brune, Science **344**, 988 (2014).
[33] G. H. O. Daalderop, P. J. Kelly, and M. F. H. Schuurmans, Phys. Rev. B **41**, 11919 (1990).
[34] R. Wu and A. J. Freeman, J. Magn. Magn. Mater. **200**, 498 (1999).
[35] P. Blaha, K. Schwarz, G. K. H. Madsen, D. Kvasnicka, and J. Luitz, computer code WIEN2K, Technische Universität, Wien, Austria, 2001.
[36] J. Kuneš, T. Jeong, and W. E. Pickett, Phys. Rev. B **70**, 174510 (2004); D. J. Singh, J. Appl. Phys. **79**, 4818 (1996); A. T. Zayak, X. Huang, J. B. Neaton, and K. M. Rabe, Phys. Rev. B **77**, 214410 (2008); X. Wan, J. Zhou, and J. Dong, Europhys. Lett. **92**, 57007 (2010).
[37] D. D. Koelling and B. N. Harmon, J. Phys. C **10**, 3107 (1977).
[38] V. I. Anisimov, F. Aryasetiawan, and A. I. Lichtenstein, J. Phys. Condens. Matter **9**, 767 (1997).
[39] R. Arita, J. Kuneš, A. V. Kozhevnikov, A. G. Eguiluz, and M. Imada, Phys. Rev. Lett. **108**, 086403 (2012).
[40] A. R. Macintosh and O. K. Andersen, in *Electrons at the Fermi Surface*, edited by M. Springford (Cambridge University, Cambridge, England, 1980).
[41] M. Weinert, R. E. Watson, and J. W. Davenport, Phys. Rev. B **32**, 2115 (1985).
[42] J. Samuel Smart, *Effective Field Theories of Magnetism* (W. B. Sauders Company, Philadelphia & London, 1966).
[43] I. Dzyaloshinskii, J. Phys. Chem. Solids **4**, 241 (1958).
[44] T. Moria, Phys. Rev. **120**, 91 (1960).
[45] M.-H. Whangbo, H.-J. Koo, and D. Dai, J. Solid State Chem. **176**, 417 (2003).
[46] D. Dai, H. J. Xiang, and M.-H. Whangbo, J. Comput. Chem. **29**, 2187 (2008).
[47] S. Baumann, F. Donati, S. Stepanow, S. Rusponi, W. Paul, S. Gangopadhyay, I. G. Rau, G. E. Pacchioni, L. Gragnaniello, M. Pivetta, J. Dreiser, C. Piamonteze, C. P. Lutz, R. M. Macfarlane, B. A. Jones, P. Gambardella, A. J. Heinrich, and H. Brune, Phys. Rev. Lett. **115**, 237202 (2015).
[48] X. Ou, H. Wang, F. Fan, Z. Li, and H. Wu, Phys. Rev. Lett. **115**, 257201 (2015).
[49] X. Ming, C. Autieri, K. Yamauchi, and S. Picozzi, Phys. Rev. B **96**, 205158 (2017).
[50] G. Kresse and J. Furthmüller, Comput. Mater. Sci. **6**, 15 (1996).
[51] G. Kresse and J. Furthmüller, Phys. Rev. B **54**, 11169 (1996).
[52] G. Kresse and D. Joubert, Phys. Rev. B **59**, 1758 (1999).
[53] A. Togo, F. Oba, and I. Tanaka, Phys. Rev. B **78**, 134106 (2008).